Chinese Chemical Letters 34 (2023) 107282

Contents lists available at ScienceDirect

Chinese Chemical Letters

journal homepage: www.elsevier.com/locate/cclet

Vacancy-enhanced Mo-N_2 interaction in $MoSe_2$ nanosheets enables efficient electrocatalytic NH_3 synthesis

Shuhong Wu[a,b], Meng Zhang[c], Shengmei Huang[c], Lihai Cai[d,*], Dannong He[a], Yitao Liu[b,c,*]

[a] School of Materials Science and Engineering, Shanghai Jiao Tong University, Shanghai 200240, China
[b] National Engineering Research Center for Nanotechnology, Shanghai 200240, China
[c] Innovation Center for Textile Science and Technology, Donghua University, Shanghai 200051, China
[d] Institute of Systems Engineering, Academy of Military Sciences, Beijing 102300, China

ARTICLE INFO

Article history:
Received 12 October 2021
Revised 7 January 2022
Accepted 1 March 2022
Available online 4 March 2022

Keywords:
$MoSe_2$ nanosheets
Doping
Se vacancies
Mo–N_2 interaction
Electrocatalysis
NH_3 synthesis

ABSTRACT

NH_3 plays an essential role in human life since it is an important raw material for fertilizers, plastics and rubbers production. As an NH_3 synthesis technology under ambient conditions, electrocatalytic N_2 reduction reaction (NRR) has great potential to replace the energy-intensive Haber-Bosch process. The key of electrocatalytic NRR is the exploration of efficient catalysts. Transition metal Mo is promising since it exists naturally in nitrogenase due to the unique Mo-N_2 interaction; particularly in the form of 2D material such as $MoSe_2$, the surface area is maximized for more active sites. However, the NRR performance of $MoSe_2$ is still unsatisfactory because Mo is only exposed at the semi-open edge, and the electronegative Se-mantled surface area remains inaccessible to N_2. Herein, we propose a simple and effective strategy to create high-concentration Se vacancies in $MoSe_2$ through heteroatom doping induced lattice strain, which effectively enhances the Mo-N_2 interaction on the surface area. In result, high NH_3 yield (3.04×10^{-10} mol s^{-1} cm^{-2}) and Faraday efficiency (21.61%) are attained at –0.45 V *vs.* RHE in 0.1 mol/L Na_2SO_4.

As the main end product and important intermediate, NH_3 has been widely used in the preparation of rubbers, plastics, dyes, fertilizers and medicines, which is essential to human life and economic development [1]. Furthermore, benefiting from the high weight hydrogen content (17.8 wt%) and large volumetric hydrogen energy density (12.7 MJ/L, liquid NH_3), as well as the advantages of easy handling, storage and transportation of liquefaction, NH_3 is also considered as a potential fuel and ideal green energy carrier in recent years [2]. Currently, industrial NH_3 synthesis still relies on the traditional Haber-Bosch process with the thermocatalytic conversion of N_2 and H_2 in the presence of Fe-based catalysts under harsh conditions (400–600 °C and 20–40 MPa) due to the chemical inertness of N≡N (bond energy: 941 kJ/mol) [3]. As an energy-intensive technology for NH_3 synthesis, the Haber-Bosch process accounts for more than 1% of global energy consumption each year [4]. Meanwhile, H_2 used in the Haber-Bosch process is mostly produced through the decomposition of fossil fuels, causing 3%–5% of the world's natural gas consumption and leading to 1.87 tons CO_2 byproduct for each ton of NH_3, which will further aggravate the global greenhouse effect [5]. In result, it is imperative to develop a clean, efficient and sustainable technology alternative to the Haber-Bosch process.

Among other approaches (*e.g.*, biocatalysis, photocatalysis, *etc.*) for the synthesis of NH_3 by N_2 reduction reaction (NRR) under ambient conditions, electrocatalytic NRR ($N_2 + 6H^+/e^- \rightarrow 2NH_3$) has attracted increasing attention because of the following merits: (1) about 20% higher energy efficiency than the Haber-Bosch process according to the thermodynamic prediction, (2) application of renewable energy resources (solar, wind, and hydro) as the driving force for electrocatalytic NRR, (3) elimination of fossil fuels as the H_2 sources *via* an oxidation reaction at the anode for H^+, and (4) modularity, scalability and on-site, on-demand NH_3 generation of the electrochemical systems [6–8]. Benefiting from the merits mentioned above, electrocatalytic NRR has great potential to replace the Haber-Bosch process. However, the industrial application of electrocatalytic NRR is still plagued by some problems such as sluggish kinetics for N_2 adsorption and N≡N bond rupture which result in large overpotentials and low reaction rates, and the competition from H_2 evolution reaction (HER) which leads to a low Faraday efficiency (FE) [9]. Under these circumstances, the focus of current research is to design and develop advanced catalysts to improve the activity and selectivity of electrocatalytic NRR [10].

Over the past decades, 2D transition metal dichalcogenides (TMDs) have been extensively studied in catalysis, energy storage,

* Corresponding authors.
E-mail addresses: lihai96@163.com (L. Cai), liu-yt03@dhu.edu.cn (Y. Liu).

https://doi.org/10.1016/j.cclet.2022.03.005
1001-8417/

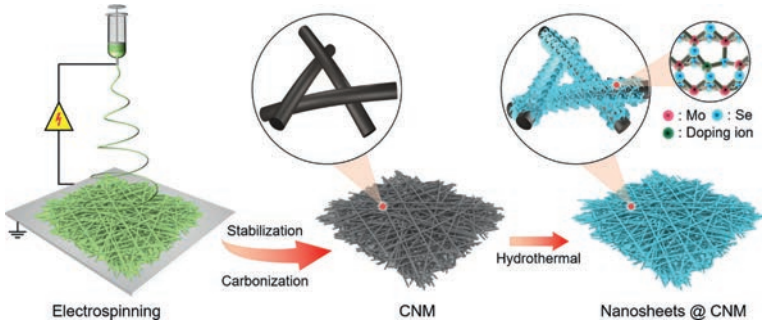

Fig. 1. Schematic representation of the synthesis process of Zr-$MoSe_2$ nanosheets@CNM through electrospinning of a PAN NM, conversion to a CNM, and hydrothermal synthesis of $MoSe_2$ nanosheets in the presence of Zr^{4+} doping ions.

and optoelectronics due to their large surface area, economic feasibility, simple preparation and chemical stability [11,12]. Among them, 2D Mo-based TMDs such as MoS_2 have attracted particular attention as NRR catalysts since Mo provides the pivotal active center for N_2 fixation in natural nitrogenase due to unique Mo-N_2 interaction [13,14]. Compared to MoS_2, $MoSe_2$ may have better electrochemical properties due to lower bandgap and higher conductivity [15]. As such, we explored the NRR performance of $MoSe_2$ in our previous work; however, it was found to be unsatisfactory because the active center Mo was only exposed at the semi-open edge, and the electronegative Se-mantled surface area remained inaccessible to N_2 [16]. Hence, basal plane activation through vacancy engineering has become an important strategy to improve the NRR performance by regulating the charge transport and surface adsorption capacity [17]. For example, Liu *et al.* synthesized vacancy-rich $ReSe_2$ through high-temperature annealing in an inert atmosphere, and found that the introduction of Se vacancies could modulate the electronic structures of $ReSe_2$ and enhanced its NRR performance [18]. However, this process was sophisticated, and the vacancy concentration was still limited.

Herein, we propose a simple and effective strategy to create high-concentration Se vacancies in 2D $MoSe_2$ through heteroatom doping induced lattice strain. At first, $MoSe_2$ nanosheets (with and without heteroatom) are facilely synthesized on a conductive matrix, *i.e.*, a carbon nanofibrous membrane (CNM) by a one-step hydrothermal method. Considering Zr^{4+} has the same (and unchangeable) valence state as Mo^{4+}, and its ionic radius (0.72 Å) is somewhat smaller than that of Mo^{4+} (0.79 Å), we expect it can enter the hexagonal lattice of $MoSe_2$ and generate lattice strain substantially [19,20]. In result, abundant Se vacancies are created, as characterized by X-Ray diffraction (XRD), electron paramagnetic resonance (EPR), and X-ray photoelectron spectroscopy (XPS). The vacancy-rich $MoSe_2$ exhibits enhanced Mo-N_2 interaction than neat $MoSe_2$ nanosheets, delivering an NH_3 yield of 3.04×10^{-10} mol s^{-1} cm^{-2} and an FE of 21.61% at –0.45 V *vs.* RHE in 0.1 mol/L Na_2SO_4. This strategy may pave an avenue to a new type of high-performance catalysts toward NRR.

The schematic representation of the synthesis process of $MoSe_2$ and Zr-$MoSe_2$ nanosheets@CNM is shown in Fig. 1. Firstly, a homogeneous solution with a polyacrylonitrile (PAN) content of 13 wt% was sucked into a syringe and fabricated into a PAN nanofibrous membrane (PAN NM) through an electrospinning progress. Then, the PAN NM was stabilized in air, followed by carbonization in N_2 to obtain a CNM. Finally, $MoSe_2$ or Zr-$MoSe_2$ nanosheets were grown on the surface of individual carbon nanofibers by a hydrothermal process (in the absence or presence of Zr^{4+}). As shown in Fig. S1 (Supporting information), the PAN nanofibers have a smooth surface with an average diameter of around 306 nm, and are connected with each other to form a 3D porous network. After stabilization and carbonization, the average diameter of the resultant carbon nanofibers decreases to 235 nm because of the entropic shrinkage and chemical shrinkage [21]. As can be seen from the field-emission scanning electron microscopy (FESEM) images in Figs. 2a and b, both nanofibers have a core-shell structure with the carbon nanofiber skeleton uniformly decorated with nanosheets after the hydrothermal process. From the enlarged view of individual nanofibers in the insets of Figs. 2a and b, the nanosheets grow perpendicularly and form channels with open spaces on the surface of individual carbon nanofibers, which is helpful to promote the electrochemical reaction by storing the electrolyte and shortening the diffusion path of ions [22]. Taking Zr-$MoSe_2$ nanosheets@CNM as the example, the average thickness of the shell is around 125.5 nm from the distribution of fiber diameters in Fig. S1. The high-resolution transmission electron microscopy (HRTEM) image in Fig. 2c shows that the nanosheets have an interlayer distance of 0.65 nm corresponding to the (002) plane of 2H-$MoSe_2$ [23]. The electron dispersion spectroscopy (EDS) images of Zr-$MoSe_2$ nanosheets@CNM in Fig. 2d reveals the homogeneous distribution of Mo, Se and Zr elements, further proving the successful synthesis of Zr-$MoSe_2$ nanosheets on the carbon nanofiber.

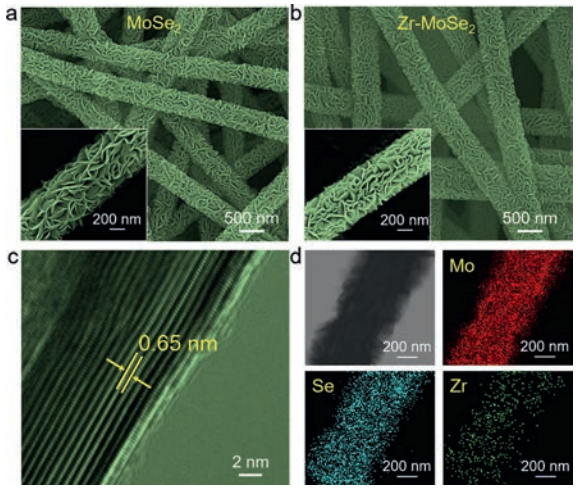

Fig. 2. FESEM images of (a) $MoSe_2$ and (b) Zr-$MoSe_2$ nanosheets@CNM. (c) HRTEM and (d) EDS images of Zr-$MoSe_2$ nanosheets. The insets in (a) and (b) are enlarged FESEM images of individual nanofibers.

In order to determine the presence of Se vacancies in Zr-$MoSe_2$ nanosheets@CNM, XRD, EPR and XPS measurements were performed. As shown in Fig. S2 (Supporting information), all the diffraction peaks correspond to 2H-$MoSe_2$ (JCPDF card No. 29–0941) and no secondary phases can be detected in Zr-$MoSe_2$ nanosheets@CNM, implying new compounds were not formed. From the enlarged view of XRD patterns at 10°–20° in Fig. 3a,

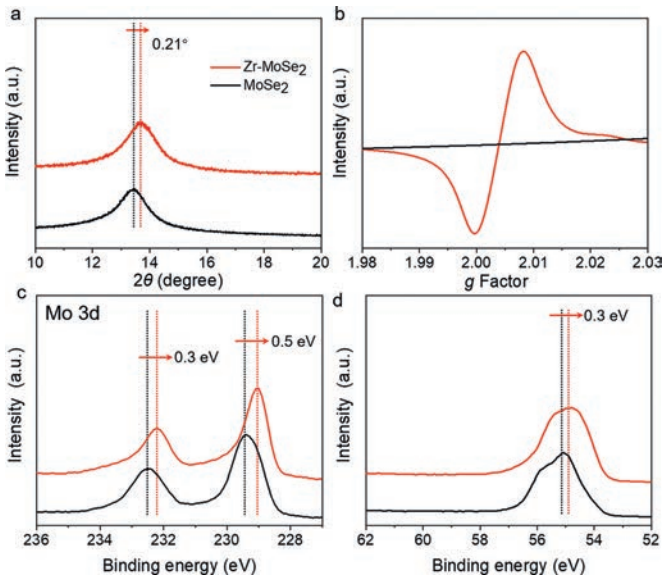

Fig. 3. (a) Enlarged view of XRD patterns in 10°–20° range, (b) EPR spectra, (c) Mo 3d XPS spectra, and (d) Se 3d XPS spectra of $MoSe_2$ and Zr-$MoSe_2$ nanosheets@CNM.

slight deviation of the (002) diffraction peak can be observed in Zr-$MoSe_2$ nanosheets@CNM due to lattice distortion. Note that Zr^{4+} with a smaller radius brings about a shrinkage of the $MoSe_2$ lattice, leading to the higher shift of 2θ degree [24]. An obvious shift of 0.21° caused by the same valance state and suitable size between Zr^{4+} and Mo^{4+} is favorable for the replacement of Mo^{4+} by Zr^{4+} in the similar crystal structure and the production of abundant Se vacancies [25,26]. Compared to $MoSe_2$ nanosheets@CNM, a stronger EPR signal ($g = 2.003$) caused by the trapping of electrons in the Se vacancies of Zr-$MoSe_2$ nanosheets@CNM can be observed in Fig. 3b, further verifying the existence of a high concentration of Se vacancies [27]. Meanwhile, when Zr^{4+} is incorporated in the $MoSe_2$ nanosheets, the XPS spectra of Mo $3d_{3/2}$ and Mo $3d_{5/2}$ (Fig. 3c) as well as Se 3d (Fig. 3d) shift to lower binding energies and provide another proof of the presence of Se vacancies and Mo^{3+} due to the decreased electron density around Mo (Fig. S3 in Supporting information) [28,29]. Furthermore, from the XPS spectrum of Zr 3d in Fig. S4 (Supporting information), we can conclude that Zr^{4+} is indeed incorporated into the lattice of the $MoSe_2$ nanosheets [30]. The presence of Se vacancies can be directly observed under high-angle annular dark-field scanning transmission electron microscopy (HAADF-STEM), where more dark dots (missing anions) occur in the Zr-$MoSe_2$ nanosheets@CNM (Fig. S5 in Supporting information).

As shown in Fig. S6 (Supporting information), the Zr-$MoSe_2$ nanosheets@CNM after the hydrothermal process can still be bent attributed to its excellent mechanical properties, which can serve as a self-supporting catalyst. The NRR performance was tested in a three-electrode system in an H-type electrolysis cell with a Nafion 212 membrane as the separator. According to the linear sweep voltammetry (LSV) curves in Fig. S7 (Supporting information), the current density in N_2-saturated 0.1 mol/L Na_2SO_4 electrolyte is larger than that in Ar-saturated electrolyte between –0.8 V *vs.* RHE and –0.2 V *vs.* RHE, implying the effective N_2 reduction of Zr-$MoSe_2$ nanosheets@CNM [31]. The chronoamperometric curves at different potentials are shown in Fig. 4a, and no obvious fluctuation in the current can be observed, indicating good stability during the electrocatalytic process [32,33]. The indophenol blue method was adopted to detect the concentration of NH_3 at different potentials. According to the standard curves and UV–vis absorption spectra of electrolyte stained with indophenol blue indicator after 2 h reaction in Fig. S8 (Supporting information), the NH_3 yield and FE can be calculated. As plotted in Fig. 4b, the highest NH_3 yield (3.04×10^{-10} mol s^{-1} cm^{-2}) and FE (21.61%) occur at –0.45 V *vs.* RHE for Zr-$MoSe_2$ nanosheets@CNM. In contrast, the highest NH_3 yield and FE of $MoSe_2$ nanosheets@CNM occur at –0.55 V *vs.* RHE, being 1.12×10^{-10} mol s^{-1} cm^{-2} and 5.96%, respectively. Moreover, the NRR performance of Zr-$MoSe_2$ nanosheets@CNM is among the best when compared to $MoSe_2$ or MoS_2-based catalysts reported elsewhere [13,16,34-42], due to the abundant Se vacancies generated by Zr^{4+} doping (Table S1 in Supporting information). Considering the stability of catalysts is a critical parameter in practical applications, cyclic and long-time electrolysis tests for Zr-$MoSe_2$ nanosheets@CNM at –0.45 V *vs.* RHE were as-

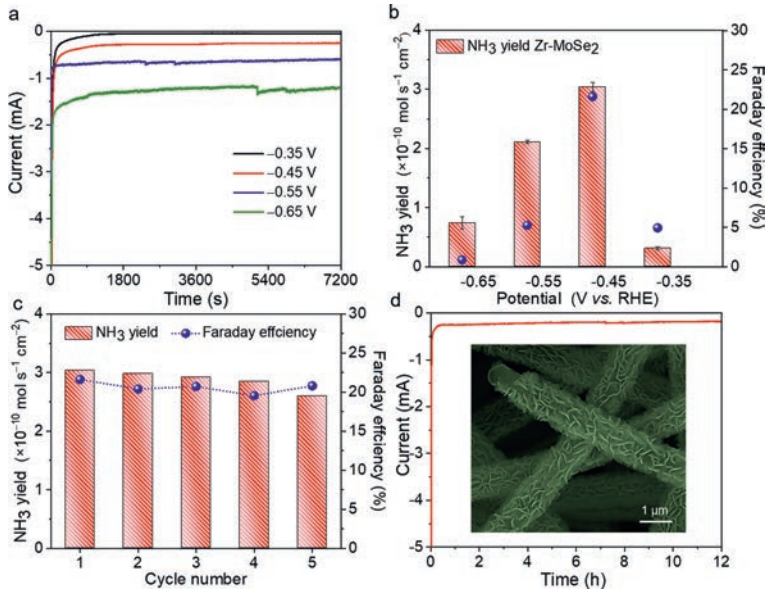

Fig. 4. (a) Chronoamperometric curves and (b) NH_3 yield and FE of Zr-$MoSe_2$ nanosheets@CNM at different potentials (V *vs.* RHE). (c) NH_3 yield and FE of Zr-$MoSe_2$ nanosheets@CNM at –0.45 V *vs.* RHE in 5 repeated cycles. (d) Chronoamperometric curve of Zr-$MoSe_2$ nanosheets@CNM at –0.45 V *vs.* RHE for 12 h and the corresponding FESEM image after the long-term durability test.

sessed. As observed in Fig. 4c, the NH_3 yield and FE do not significantly change during 5 consecutive cyclic tests, showing the excellent recyclability for N_2 reduction. Besides, no obvious fluctuation of current density (Fig. 4d) and well-preserved morphology of nanosheets (inset of Fig. 4d) after 12 h electrolysis suggest that Zr-$MoSe_2$ nanosheets@CNM has a good electrochemical durability. The possible byproduct N_2H_4 was not detected after 12 h electrolysis by the Watt and Chrisp method (Fig. S9 in Supporting information). Note that these values are significantly lower than those of Zr-$MoSe_2$ nanosheets@CNM, proving that the higher vacancy concentration is beneficial to lower the reaction overpotential and improve the performance of electrocatalytic NRR [43–45].

In conclusion, this work demonstrates a simple and effective strategy to create high-concentration Se vacancies in $MoSe_2$ through Zr^{4+} doping induced lattice strain, aiming to improve the electrocatalytic NRR performance. Zr-$MoSe_2$ nanosheets@CNM with good self-supporting properties is synthesized by a hydrothermal process. Abundant Se vacancies are created, as characterized by XRD, EPR and XPS. The vacancy-rich $MoSe_2$ exhibits enhanced Mo-N_2 interaction, delivering an NH_3 yield of 3.04×10^{-10} mol s^{-1} cm^{-2} and an FE of 21.61% in 0.1 mol/L Na_2SO_4 with excellent stability for electrocatalytic NRR.

Declaration of competing interest

The authors declare no competing interests.

Acknowledgments

This work was financially supported by the National Natural Science Foundation of China (No. 52173055), the Natural Science Foundation of Shanghai (No. 19ZR1401100), the Fundamental Research Funds for the Central Universities and DHU Distinguished Young Professor Program (No. LZA2020001).

Supplementary materials

Supplementary material associated with this article can be found, in the online version, at doi:10.1016/j.cclet.2022.03.005.

References

[1] Y. Wang, Q. Li, W. Shi, P. Cheng, Chin. Chem. Lett. 31 (2020) 1768–1772.
[2] M. Aziz, A.T. Wijayanta, A.B.D. Nandiyanto, Energies 13 (2020) 3062.
[3] G. Qing, R. Ghazfar, S.T. Jackowski, et al., Chem. Rev. 120 (2020) 5437–5516.
[4] F. Lai, N. Chen, X. Ye, et al., Adv. Funct. Mater. 30 (2020) 1907376.
[5] M. Wang, M.A. Khan, I. Mohsin, et al., Energy Environ. Sci. 14 (2021) 2535–2548.
[6] H. Shen, C. Choi, J. Masa, et al., Chem 7 (2021) 1708–1754.
[7] M. Zhang, Y. Wang, Y. Zhang, et al., Angew. Chem. Int. Ed. 59 (2020) 23252–23260.
[8] Y.T. Liu, L. Tang, J. Dai, J. Yu, B. Ding, Angew. Chem. Int. Ed. 59 (2020) 13623–13627.
[9] A.R. Singh, B.A. Rohr, M.J. Statt, et al., ACS Catal. 9 (2019) 8316–8324.
[10] L. Shi, Y. Yin, S. Wang, H. Sun, ACS Catal. 10 (2020) 6870–6899.
[11] H. Wang, C. Li, P. Fang, Z. Zhang, J.Z. Zhang, Chem. Soc. Rev. 47 (2018) 6101–6127.
[12] X. Zhu, L. Mo, Y. Wu, et al., Compos. Commun. 9 (2018) 86–91.
[13] L. Zhang, X. Ji, X. Ren, et al., Adv. Mater. 30 (2018) 1800191.
[14] J. Guo, T.T. Tsega, I.U. Islam, et al., Chin. Chem. Lett. 31 (2020) 2487–2490.
[15] P. Yang, Z. Wu, Y. Jiang, et al., Adv. Energy Mater. 8 (2018) 1870116.
[16] M. Zhang, L. Zhang, S. Huang, et al., Appl. Catal. B: Environ. 292 (2021) 120175.
[17] F. Yuan, R. Sun, L. Fu, G. Zhao, Chin. Chem. Lett. 33 (2022) 2188–2194.
[18] F. Lai, W. Zong, G. He, et al., Angew. Chem. Int. Ed. 59 (2020) 13320–13327.
[19] A.A. Tedstone, D.J. Lewis, P. O'Brien, Chem. Mater. 28 (2016) 1965–1974.
[20] M.S.L. Aparicio, M.A. Ocsachoque, D. Gazzoli, I.L. Botto, I.D. Lick, Catalysts 7 (2017) 293.
[21] I.M. Alarifi, A. Alharbi, W.S. Khan, R. Asmatulu, J. Appl. Polym. Sci. 133 (2016) 43235.
[22] D. Ji, S. Peng, L. Fan, et al., J. Mater. Chem. A 5 (2017) 23898–23908.
[23] S. Huang, M. Zhang, Y.T. Liu, J. Phys.: Conf. Ser. 1948 (2021) 012222.
[24] Y.S. Jeon, H.W. Seo, S.H. Kim, Y.K. Kim, J. Nanosci. Nanotechnol. 16 (2016) 4814–4819.
[25] N. Cao, Z. Chen, K. Zang, et al., Nat. Commun. 10 (2019) 2877.
[26] M.J. Mleczko, C. Zhang, H.R. Lee, et al., Sci. Adv. 3 (2017) e1700481.
[27] H. He, D. Huang, Q. Gan, et al., ACS Nano 13 (2019) 11843–11852.
[28] Z. Luo, Y. Ouyang, H. Zhang, et al., Nat. Commun. 9 (2018) 2120.
[29] D. Xiao, Q. Ruan, D.L. Bao, et al., Small 16 (2020) 2001470.
[30] J. Song, J. Dai, P. Zhang, et al., Nano Res. 14 (2021) 1479–1487.
[31] L. Yang, T. Wu, R. Zhang, et al., Nanoscale 11 (2019) 1555–1562.
[32] Y.T. Liu, X. Chen, J. Yu, B. Ding, Angew. Chem. Int. Ed. 58 (2019) 18903–18907.
[33] W. Xu, M. Zhang, C. Ma, S. Wu, Y.T. Liu, Appl. Catal. B: Environ. 308 (2022) 121225.
[34] L. Yang, H. Wang, X. Wang, et al., Inorg. Chem. 59 (2020) 12941–12946.
[35] Z. Wu, R. Zhang, H. Fei, et al., Appl. Surf. Sci. 532 (2020) 147372.
[36] X. Li, T. Li, Y. Ma, et al., Adv. Energy Mater. 8 (2018) 1801357.
[37] J. Zhang, X. Tian, M. Liu, et al., J. Am. Chem. Soc. 141 (2019) 19269–19275.
[38] H. Su, L. Chen, Y. Chen, et al., Angew. Chem. Int. Ed. 59 (2020) 20411–20416.
[39] J. Liang, S. Ma, J. Li, et al., J. Mater. Chem. A 8 (2020) 10426–10432.
[40] X. Xu, X. Tian, B. Sun, et al., Appl. Catal. B: Environ. 272 (2020) 118984.
[41] J. Chen, C. Zhang, M. Huang, et al., Appl. Catal. B: Environ. 285 (2021) 119810.
[42] X. Zi, J. Wan, X. Yang, et al., Appl. Catal. B: Environ. 286 (2021) 119870.
[43] F. Lai, J. Feng, X. Ye, et al., J. Mater. Chem. A 8 (2020) 1652–1659.
[44] Y.T. Liu, D. Li, J. Yu, B. Ding, Angew. Chem. Int. Ed. 58 (2019) 16439–16444.
[45] L. Tang, J. Dai, Y.T. Liu, et al., Compos. Commun. 23 (2021) 100551.